Modelling of the test of the JT-60SA HTS current leads

A Zappatore[1], R Heller[2], L Savoldi[1] and R Zanino[1]

[1] NEMO Group, Dipartimento Energia, Politecnico di Torino, Italy
[2] Karlsruhe Institute of Technology, Germany

Corresponding author e-mail: Laura Savoldi, email address: laura.savoldi@polito.it, postal address: Dipartimento Energia, Politecnico di Torino, Corso Duca degli Abruzzi 24, 10129 Torino, Italy.

Abstract

The CURLEAD code, which was developed at the Karlsruhe Institute of Technology (KIT), implements an integrated 1D transient model of a high temperature superconducting (HTS) current lead (CL) including the room termination (RT), the meander-flow type heat exchanger (HX), and the HTS module. CURLEAD was successfully used for the design of the 70 kA ITER demonstrator and of the W7-X and JT-60SA CLs. Recently the code was successfully applied to the prediction and analysis of steady state operation of the ITER correction coils (CC) HTS CL. Here the steady state and pulsed operation of the JT-60SA HTS CLs are analysed, which requires also the modelling of the HX shell and of the vacuum shell, which was not present in the ITER CC. The CURLEAD model extension is presented and the capability of the new version of CURLEAD to reproduce the transient experimental data of the JT-60SA HTS CL is shown. The results obtained provide a better understanding of key parameters of the CL, among which the temperature evolution at the HX-HTS interface, the GHe mass flow rate needed in the HX to achieve the target temperature at that location and the heat load at the cold end.

1. Introduction

Current leads are devices adopted to connect a power supply, typically at room temperature, to various clients, usually at cold (cryogenic) temperatures. High temperature superconducting current leads (HTS-CL) cooled by He gas have been designed since more than 20 years [1] and used for supplying the electrical current to superconducting magnets in both fusion devices [2], [3] and particle accelerators [4]. Other concepts have been developed in the past, like the so-called conventional CLs, which are not equipped with a superconductor, leading to various pros and cons with respect to the binary (HTS) CLs which are discussed in detail e.g. in [5], [6], or HTS-CL cooled by different fluids, as e.g. Nitrogen [7], [8].

The Karlsruhe Institute of Technology (KIT) is responsible for the construction and test of the HTS-CL for the ITER satellite tokamak JT-60SA [9]: 6 CLs with a maximum current of 25.7 kA for the toroidal field (TF) coils and 20 CLs with a maximum current of 20 kA for the central solenoid (CS) and poloidal field (PF) coils.

While the TF coils of JT-60SA operate at constant electrical current, the CLs for the CS and PF coils work with time varying currents depending on the specific plasma scenario. Therefore, the performance in pulsed operation of the latter CLs was tested through a representative series of current pulses.

A reliable numerical tool able to accurately predict the CL performance is important for its design and optimization [10]-[12], but also for the analysis of CL test results, aiming at an optimized design. It has been observed, in fact, that discrepancies were present between measured data and design values of the JT-60SA CL, which could not be easily explained, in particular concerning two main parameters that determine the performance of the HTS-CL, and namely:

- the helium mass flow rate required for cooling the HX, which needs to be minimized, to reduce the refrigerator power required to operate the lead, for a specific value of current, keeping the temperature of the HTS module in a suitable range in order to operate correctly;

- the heat load at 4.5 K, which has to be small, still coexisting with the need to transport several kiloamperes. The requirement on the heat load at low temperature would require, for example, the minimization of the cross section of the lead, while that of the transport current would drive the geometry in the opposite direction: an optimal design needs to find the best compromise between those two aspects.

The modeling performed in the recent past, using the original version of the CURLEAD code, showed a good capability to reproduce the steady state operation of the prototype CLs for the ITER CC [13].

However, the KIT CL design as presented in more detail in section 2 differs from that of the prototype CLs for the ITER CC, including for instance a vacuum shell, where the entire CL is contained, which was not present in the ITER CC CL design. These shells can strongly affect the heat load at 4.5 K. Numerical tools, such as the CURLEAD code, did not include such shells in the model so far, so that the quality of the agreement with the available experimental data (copper temperatures, mass flow rates), predicted in steady state for the ITER CC CL prototypes, does not imply the same good agreement for the *steady-state operation* of the JT-60SA CL. Furthermore, since transient (pulsed) current operation is typical of several magnets, the need is there to correspondingly assess the code reliability in *transient* simulations. In this paper, we show how we enable the CURLEAD model to properly model the steady-state and transient operation of KIT CLs, such as the JT-60SA ones.

The paper is organized as follows: first, the JT-60SA CL layout is presented, with emphasis on the metal shells that constitutes a major difference with respect to the ITER CC CL [13]. The corresponding new ingredients in the CURLEAD model are then described and the resulting new version of the code is applied to the analysis of both steady state and transient operation of the JT-60SA CLs. Finally, the simulation results are discussed and compared to the available measurements, showing that the model is adequate to reproduce the JT-60SA CL steady state and transient behavior.

2. HTS current leads for JT-60SA

The HTS-CL for JT-60SA is schematically shown in figure 1 and described in [14]. It consists of three main components:
- The room temperature end, which connects the HTS-CL to the water-cooled feeder. It is equipped with resistive heaters, in order to shape the temperature gradient at the warm end to avoid, for instance, the freezing of that region.
- The copper heat exchanger (HX), encapsulated in a stainless steel shell (HX shell), covering the temperature range between room temperature and 60 K, and cooled with 50 K helium. Among the possible different alternatives (see, e.g., [8]), the HX is built according to the meander flow concept. The diameter of the copper core of the HX is not constant along the HX length: it passes from 55 mm (first 20 cm of the HX from the HTS) to 45 mm in the rest of the HX.
- The HTS module, covering the temperature range between 60 K and 4.5 K, conduction-cooled at the 4.5 K end, equipped with a copper cold end, which is connected to the superconducting feeder. The HTS module consists of a cylindrical stainless steel support structure with copper end caps. On the outer surface, grooves are cut wherein the Bi-2223/AgAu superconductor stacks manufactured by Bruker HTS are soldered. In total 60 6-fold stacks of 470 mm length for the CS/PF current leads were required. The minimum specified critical current of a stack is 430 A at 77 K and self-field. The cold end connection to the superconducting feeder is realized by a half-cylindrical copper block with inserts of Nb_3Sn wires to reduce the resistive losses, the flat surface being gold plated.

The whole CL is enclosed in a stainless steel shell (vacuum shell), which is electrically insulated at the outer surface and equipped with a G10 flange glued on the insulated tube, acting as connection to the cryostat.

In table 1 the main design parameters are summarized.

Table 1 Main Design Parameters of the HTS current leads for JT-60SA

| Parameter	CS/PF
Operation mode	pulsed
Maximum current I_{max}	20 kA
Nominal current I_{nom}	13.6 kA
Maximum stray field	33 mT
Maximum voltage during operation	10 kV
Test high voltage against ground	21 kV
HTS module	
Critical current of single tape / stack at 77 K and self-field	>110 A / >430 A
Number of tapes	360
Number of tapes in stack / stacks in panels / panels in module	6 / 5 / 12
Outer dimension of HTS module	117 mm
HTS tape cross section	3.32 cm^2
Lower end temperature	4.5 K
Maximum temperature	60 K
Stainless steel cross section	13.26 cm^2
Length of HTS stacks	470 mm
Heat exchanger HX	
Type and material of HX	Meander flow type made of E-Copper (RRR $\approx$ 50)
Diameters of Cu conductor (cold / warm end)	55/45 mm
Outer diameter of HX	120 mm
Maximum current density	12.6 A/mm^2
Length of HX	1.207 m
Temperature levels (Lower / upper end)	60 K / (290 – 320) K
He inlet temperature	(50 $\pm$ 2) K
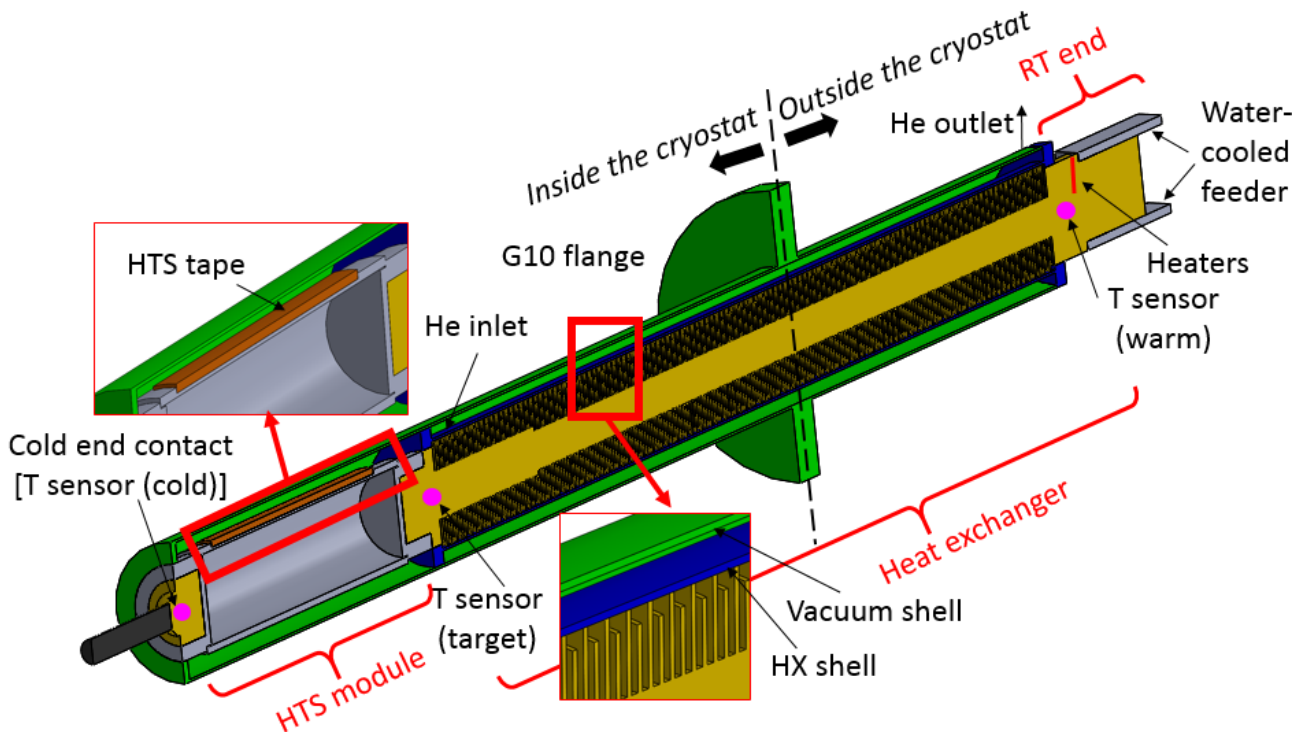
Figure 1. Main components of the JT-60SA HTS CL with a zoom of the meander flow type HX and of the HTS module in the insets below and above the CL sketch, respectively. The yellow regions are the copper parts that include the RT end and the HX. The stainless steel support (grey hollow cylinder) and one of the HTS tapes (orange) of the HTS module are represented. The position of the main temperature sensors is also indicated.

A schematic view of the connections between the shells and the copper core in the typical KIT CL design is reported in figure 2, where the main heat fluxes are also shown. In fact, both the HX and the vacuum shells, and in particular the latter, which was not present in the ITER CC CL prototype, act as thermal bridge between the environment at room temperature and the cold end of the lead.
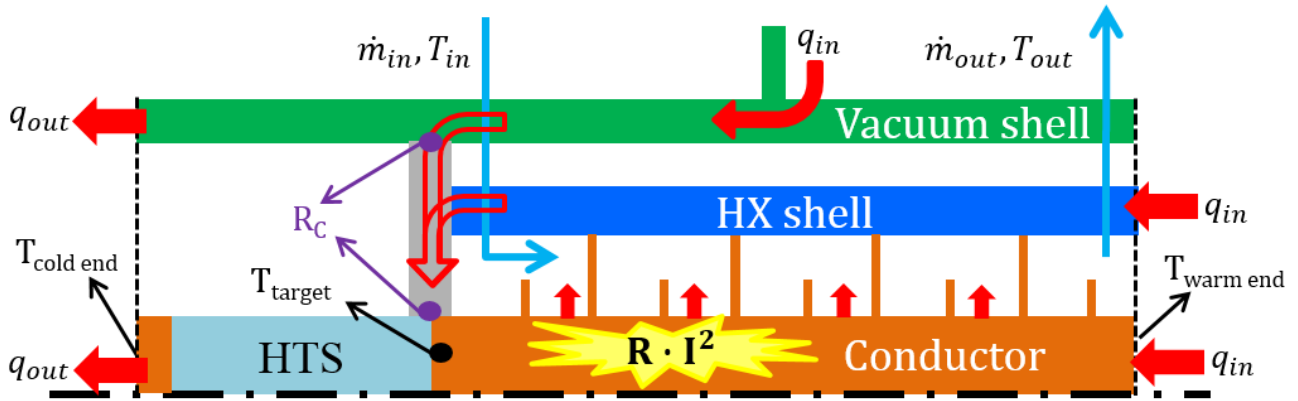

Figure 2. Simplified representation of the CL shells and of the central conductor, highlighting the relevant temperature sensor locations (black arrows) and the heat fluxes exchanged between different CL parts as well as those entering or exiting the CL (red arrows). The He path is also reported (light blue arrows) as well as the thermal contact between the shells and the conductor.

3. Tests of the JT-60SA HTS CL

3.1. Steady state tests

Steady state tests were performed at zero current as well as at 20 kA on the two twin CLs tested at the same time at the KIT premises, named from now on as CL1 and CL2. The three cases selected for the present analysis on the basis of the completeness and reliability of the respective database are listed in table 2. The target temperature is monitored by two redundant sensors, placed at the same axial position.

Table 2 Operating conditions of the steady-state tests considered in the present analysis.

Case #	Current (kA)	Operating conditions									
		RT temperature (K)		Cold end temperature (K)		He temperature (K) @ the HX inlet[&]		Target temperature (K)			
		CL1	CL2	CL1	CL2	CL1	CL2	CL1		CL2	
								Sens. 1	Sens. 2	Sens. 1	Sens. 2
1	0	290.00	289.93	6.43	6.36	50.41		63.13	63.99	63.31	63.46
2	0	290.00	289.90	6.29	6.24	50.19		58.98	59.78	59.27	59.46
3	20	290.34	290.08	7.29	7.15	49.67		58.62	59.45	57.69	57.84

[&]The measurement is performed on a single tube which is then split in two to feed the two CLs

In all the tests, the He pressure at the HX inlet was 2.4 – 2.8 bar.

3.2. Pulsed test

The only pulsed test performed on these CLs was also selected for the present analysis. The scenario consists of 7 successive identical pulses, one of which is reported in figure 3. The ramp up and ramp down rates are equal to 0.5 kA/s and -0.5 kA/s respectively.
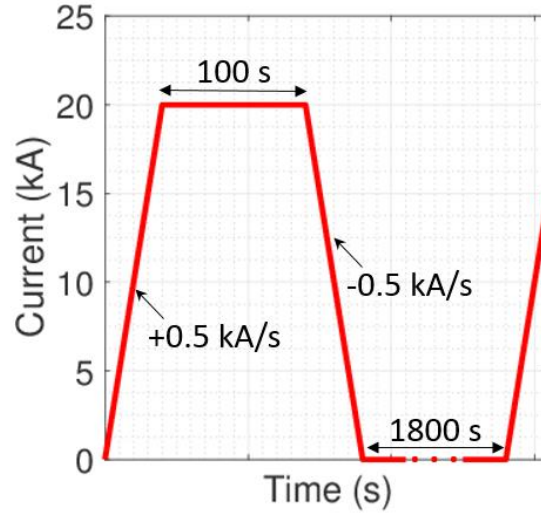

Figure 3. Pulsed current scenario performed on the JT-60SA HTS CL (the time on the x axis is not in scale).

The main features of the experimental data are shown in figure 4, showing that the main driver of the time evolution of the cold end temperature is the current behaviour (Fig. 4a), while the warm end temperature is mainly driven by the heaters power evolution (Fig. 4b). The helium mass flow rate, pressure and temperature do not experience sudden changes during the entire transient (see below). When sudden changes are present, they are caused by other factors like the dynamics of the refrigerator.
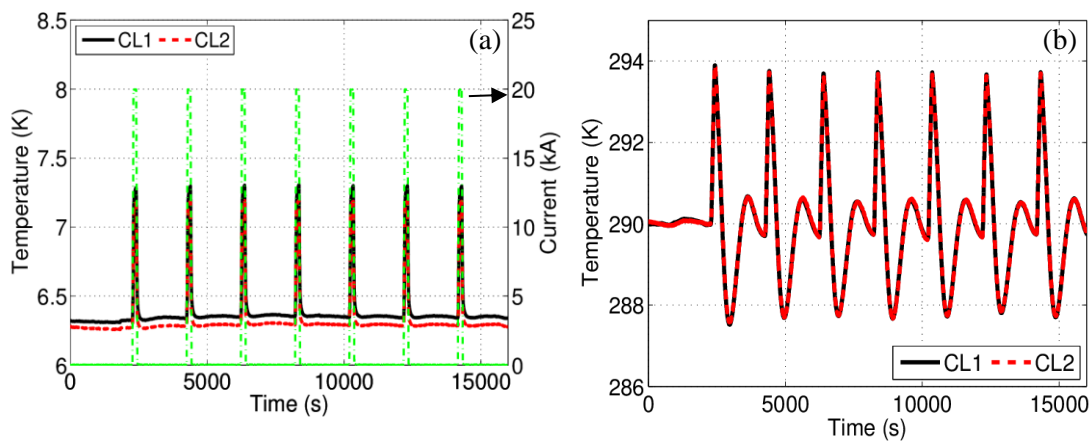

Figure 4. (a) Measured temperature at the cold end and (b) at RT temperature during the pulse test of the JT-60SA CL1 and CL2.

4. The new CURLEAD model for the KIT HTS CL

The basic features of the CURLEAD code [15], already proved to be sufficient to reproduce the steady-state operation of the ITER CC CL, have been presented in [13], and can be summarized as:
- 1D transient heat conduction equation for the Cu bar, for the entire computational domain. The heat transfer coefficient is taken from the correlations in [16], [17].

- 1D transient heat conduction equation for the region of the HTS tapes, taking into account the presence of the different materials of the HTS as well as the presence of the SS shunt on which the tapes are placed.
- 1D advection equation for the He in the HX, thermally coupled to the Cu bar. The constitutive relations for friction *f* and heat transfer coefficient *h* are taken from CFD-based correlations, see [16], [17], which account for the fluid temperature as well as for the coolant mass flow rate through the dependence of *f* and Nusselt number on the Reynolds number.

Note that the Cu bar and the HTS region are modelled accounting for cross section and material variations along the axial direction, if present. In addition, the temperature dependence of all the materials is considered by the frozen coefficients technique.

The boundary conditions for the model are: the RT temperature, the cold-end temperature, the mass flow rate, pressure and temperature at the HX inlet. The driver of the transient is mainly the transport current, even if also the time dependence of all the boundary conditions is taken into account.

Although the 1D modelling of these objects is a well-established approach in the community, we tailor here a standard 1D model to the JT-60SA CLs design, including relevant portions of the CL which strongly affect its performance, see below. Only thanks to this more detailed model, it has been possible to perform a very accurate validation, i.e. a fundamental step in judging the reliability of a numerical tool, even when the approach is rather standard. In the following sections, the details of the new ingredients added to the CURLEAD model to account for the peculiar topology of the KIT CLs are presented.

4.1. Model of the heat exchanger shell

The HX shell is the casing needed to force the GHe mass flow rate to travel along the meander-flow type heat exchanger. In the JT-60SA CLs, it consists of a 3 mm thick stainless steel (SS) hollow cylinder, which starts from the room termination (RT) and ends at the HX-HTS module interface.

This shell is modelled through a 1D heat diffusion equation, taking into account the heat transfer to the He flow on its inner side. Since a quantitative estimation of the heat transfer coefficient between the shell and the helium is rather difficult, the same value adopted for the central conductor is employed. This should be an upper bound of the heat transfer between the fluid and the shell, since the actual value of the heat transfer coefficient should be lower than the one currently employed, because the HX is designed to effectively cool the central copper conductor rather than the surrounding shell. The additional equation solved by the code along the entire HX length is therefore the standard transient heat conduction equation:

$$\rho_{SS} c_{p,SS}(T_{HX}) A \frac{\partial T_{HX}(x,t)}{\partial t} = \frac{\partial}{\partial x}\left[k_{ss}(T_{HX}) A \frac{\partial T_{HX}(x,t)}{\partial x}\right] - hP(T_{HX} - T_{He}) \tag{1}$$

where ρ_{SS} is the SS density (kg/m^3), $c_{p,SS}$ is the SS specific heat capacity (J/kg K), A is the cross-sectional area (m^2), T_{HX} is the axial temperature of the HX shell (K), k_{ss} is the SS thermal conductivity (W/m/K), h is the heat transfer coefficient (W/m^2/K), P is the wetted perimeter (m) and T_{He} is the helium temperature (K). The two ends of the HX shells are assumed to have a prescribed temperature as BC: at the warm end of the domain, the measured temperature at the RT is imposed; at the cold end, the computed local temperature of the Cu bar (see above) at each time step is applied.

The coupling of the HX shell to the rest of the CL model is done explicitly, computing, from the temperature gradient at the low temperature boundary, the heat in input at the HTS-HX interface (target region), see figure 2, which constitutes a local heat source for the Cu bar.

4.2. Model of the vacuum shell

The vacuum shell, the outermost envelope covering the CL along its entire length, is composed by a 3 mm thick inner layer of stainless steel on which a G10 insulation shell (5 mm thick) is placed. This second shell was introduced because, among other reasons, it acts as a radiative shield for the inner structures. As the name suggests, vacuum is present in the annulus between this shell and the HX one.

The shell is welded to a stainless steel ring which is brazed to the copper target region, at the same axial location where the HX shell ends. A G10 flange is placed outboard of this shell, at an axial coordinate approximately equal to half of the HX length. Therefore, the thermal bridge introduced by this shell allows the transmission of heat from the flange location at 300 K to both the target region and the cold end of the lead. Since the shell is placed outside the cryostat from the flange location up to the RT, the computational domain adopted for the vacuum shell model starts from the flange and ends at the shell cold end, which corresponds to the conductor cold end, see figure 1.

The equation introduced to compute the temperature profile of the vacuum shell all along the lead is:

$$\rho_V c_{p,V}(T_V) A \frac{\partial T_V(x,t)}{\partial t} = A \frac{\partial}{\partial x}\left[k_v(T_V)\frac{\partial T_V(x,t)}{\partial x}\right] - \frac{T_V(x,t) - T_{Cu}(x,t)}{R_C} f(x) \qquad (2)$$

where the subscript "V" stands for vacuum. The shell cross section A is the sum of the cross section of the stainless steel and of the G10 part. The properties are obtained as average on the shell cross section, i.e. the generic property Z is evaluated as $Z = \frac{1}{A}\int_{r_i}^{r_o} Z(r)\, 2\pi r dr$. Therefore, ρ_V is the average density (kg/m³), $c_{p,V}$ is the average specific heat capacity (J/kg K), T_V is the temperature of the shell (K), k_v is the average thermal conductivity (W/m K), T_{Cu} is the temperature of the copper (K), R_C is the calibrated resistance (K m/W). In addition, $f(x)$ is equal to one only at the HTS-HX interface, where the thermal contact is present, otherwise it is equal to zero.

A temperature equal to 300 K has been imposed as boundary condition at the shell warm end, while the same measured temperature used for the central conductor has been used at the shell cold end.

The terms on the right-hand side of (2) account for conduction along the shell and heat transfer to the target region of the central conductor through the thermal resistance R_C, which is hard to be evaluated a priori, since the quality of the contact between the stainless steel part of the vacuum shell and the ring that connects the shell to the HX-HTS copper interface is not known, requiring thus a dedicated calibration, see below.

In order to take into account the strong coupling between the vacuum shell and the copper (as well as between the copper and the coolant), an implicit time scheme has been introduced for the solution of the entire set of equations.

5. Calibration of the vacuum shell model

In order to calibrate the contact thermal resistance R_C for the JT-60SA CLs, one of the steady state runs at zero current (case #1), see table 2, was used. The calibration is performed on each CL, since the manufacturing process could have been not exactly the same, leading to a different thermal contact, therefore a different value of R_C. The value of R_C has been progressively increased to the value guaranteeing the best agreement between the computed and measured target temperature, see figure 5, for the experimental value of the mass flow rate. Figure 5(c) shows quantitatively the error associated to each value of R_C adopted during the calibration process. The values of R_C corresponding to the minimum error have then been frozen for all the other simulations.

An error bar associated to R_C has been computed considering the experimental error-bar associated to the measured mass flow rate, giving the lower and upper bounds reported in Table 3. These values contribute to define the error bar associated to the computed thermal-hydraulic results presented below.

Table 3 Calibrated contact thermal resistance R_C for CL1 and CL2, respectively.

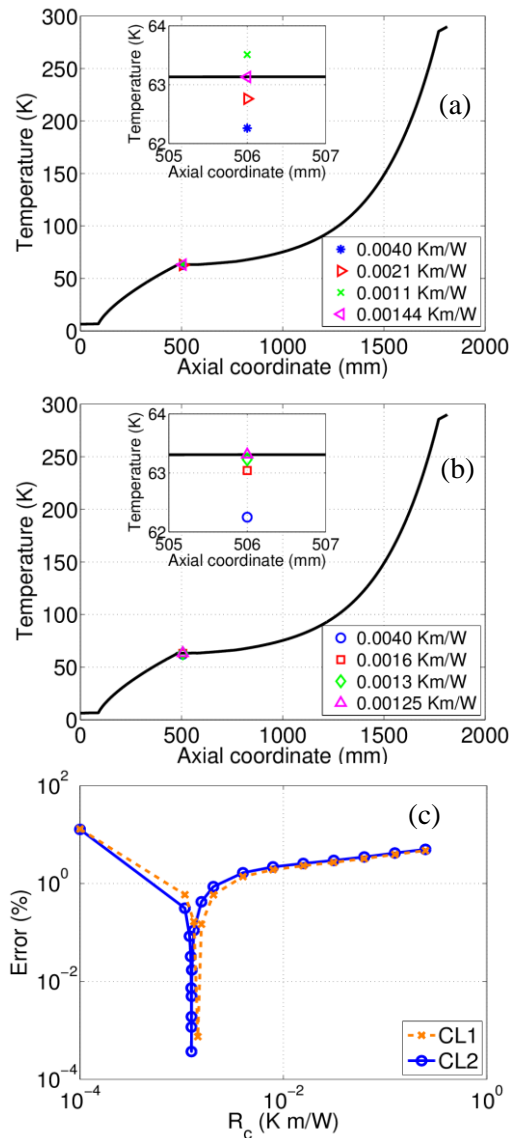|	$R_C \cdot 10^3$ (K m / W)		
	Nominal	Lower bound	Upper bound
CL1	1.44	0.39	3.85
CL2	1.25	0.37	2.98

Figure 5. Calibration of the R_C during steady state using the nominal mass flow rate (case #1): spatial temperature profile along the CL axis, with the inset that shows the variation of the computed target temperature as the thermal contact resistance is varied (symbols) in CL1 (a) and CL2 (b). Relative error between the desired target temperature and the computed one as a function of R_C (c).

6. Steady state analysis with the new model and comparison with experimental data

The two steady state tests remaining after calibration of the R_C value (i.e., cases #2 and #3 in table 2) are simulated with CURLEAD, imposing the experimental mass flow rate (this is a slightly different approach with respect to the optimization analysis performed in [13]).

In the case without current (case 2), the target temperature is well reproduced with the inclusion of the shells for both CLs. At the same time, the computed cold end heat load matches well with the measured one if shells are included (note that the heat load at the cold end is now computed as the sum of the load coming through the conductor and of the one coming through the vacuum shell). Concerning the pressure drop, a larger measured value is expected with respect to the computed one since the pressure taps are not located right at the He inlet/outlet, but upstream/downstream, respectively, including thus additional pressure losses to that just computed across the HX.

In the case with current, the comparison between CURLEAD results and measurements is performed only for CL2, since the analysis of the experimental traces shows that CL1 was not in steady state yet (not shown). The computed target temperature is reproduced within less than 1 K; also the computed heat load reproduces the experimental value within the error bar. Finally, for the pressure drop a value higher than the measured one is computed, but note that, for the case of interest the friction factor correlation adopted in the simulation is known to overestimate the one computed by CFD by ~ 28%. For this reason, the proper (larger) error bar is represented in figure 6(f).

On the other hand, if the mass flow rate is chosen as output, imposing the target temperature adopting the strategy shown in [13], the same good agreement shown here in figure 6 (a) and (b) is found.
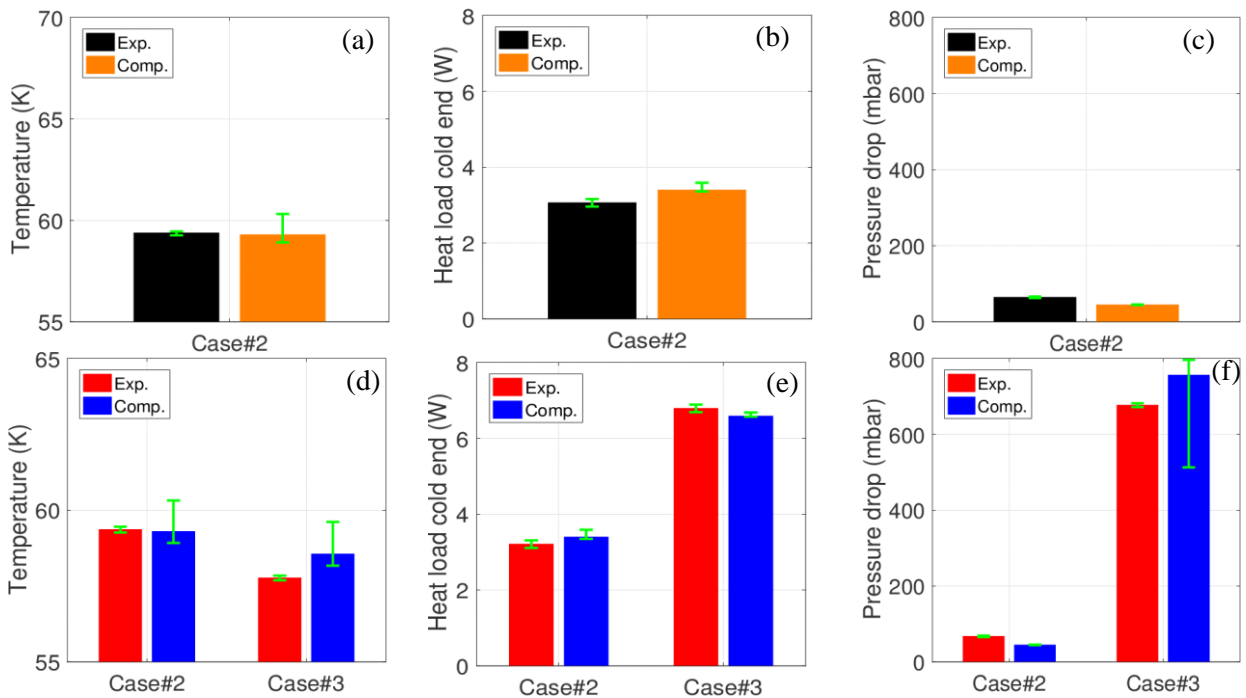

Figure 6. Comparison between experimental and computed steady state data for the CL1 (a), (b), (c) and CL2 (d), (e), (f) of target temperature (a, d), heat load at the cold end (b, e) and pressure drop across the HX (c, f).

The contribution of the two shells in terms of heat deposited/removed in the target region is mostly due to the vacuum shell while a small portion flows in the HX shell, see figure 7. Furthermore, if the two heat loads are compared to the one coming by conduction from the copper, it is evident that the presence of the vacuum shell could not be neglected. This contributes to explain the reason why the presence of the HX shell also in the prototype ITER CC CLs was not so relevant. In that case, in fact, the vacuum shell, which is the most relevant, was not present. In addition, considering the heat load reaching the CL cold end, about 20% of the total is due to the presence of the vacuum shell.
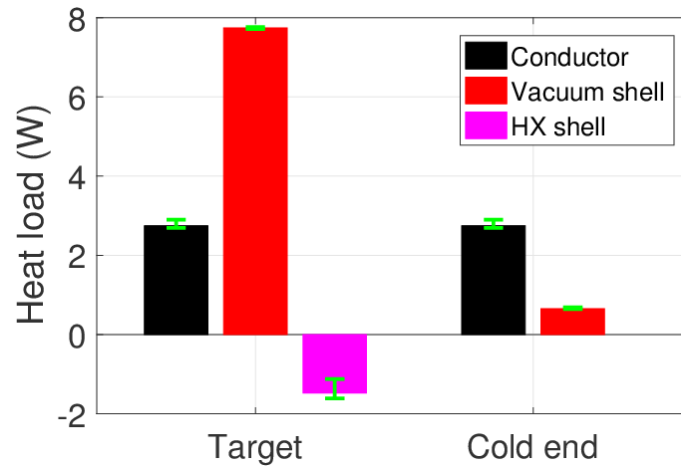
Figure 7. Total heat load deposited in the target region: contribution from the two shells and from the central copper bar; heat load at the cold end: contribution from the central copper bar and from the vacuum shell. The computed results of Case 2 for the CL2, see table 2, have been considered.

7. Simulation of pulsed operation of the JT-60SA CLs

Also in the case of the pulsed scenario, the simulation is performed using in input the measured mass flow rate evolution, and computing the target temperature, as well as the heat load. The spatial temperature profile of the shells obtained using the measurements at t = 0 s is used as initial condition in the transient simulations.

7.1. Target temperature

The computed and measured temperature profiles at the target location are reported in figure 8.
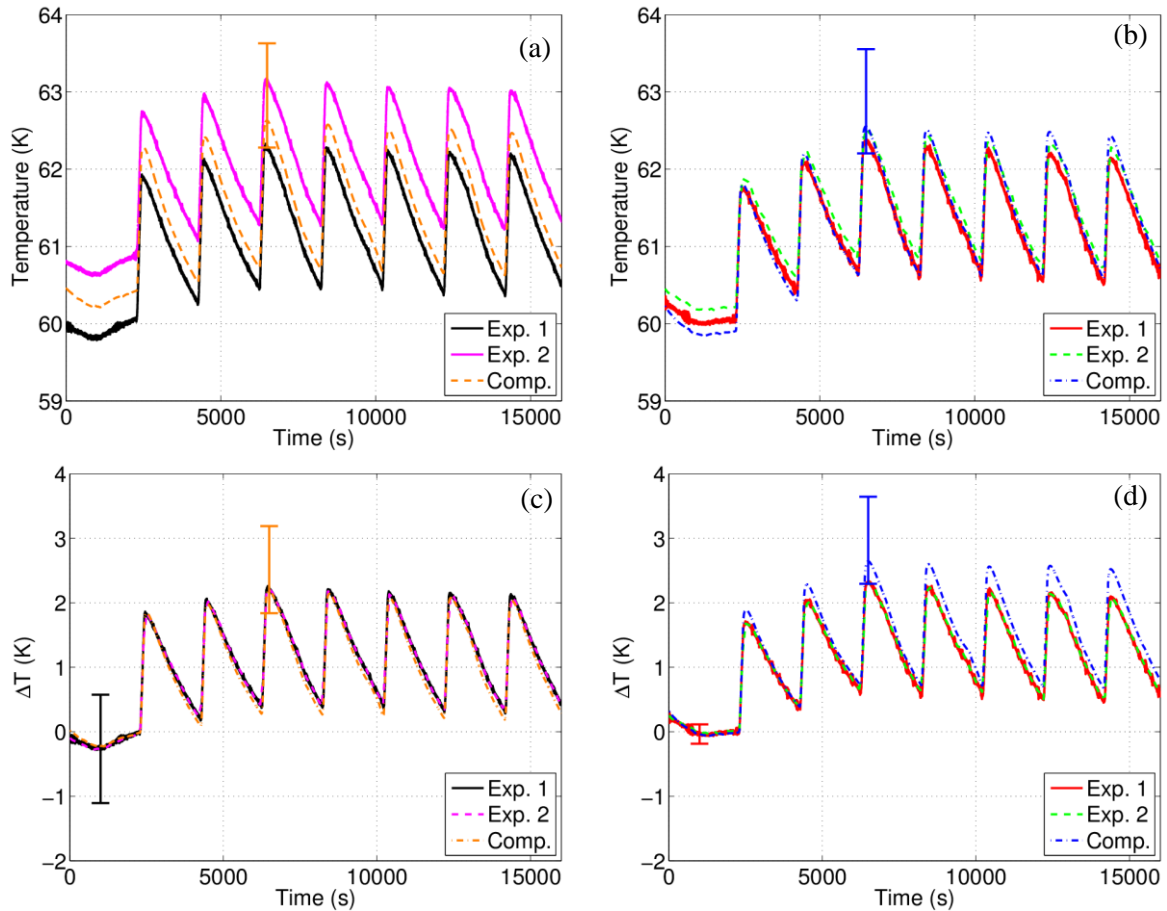
Figure 8. Simulation of the JT-60SA CLs pulsed test: comparison between experimental and computed target temperature time evolution during the entire transient (a) and when the offset is removed (c) in the JT-60SA CL1. The same results are presented for the pulsed test of the JT-60SA CL2 in (b) and (d).

The measured target temperatures show an offset of ~ 0.8 K for the CL1 and ~ 0.2 K for the CL2, but once the offset (value of the temperature at the beginning of the first pulse) is removed, the temperature difference measured by the two redundant sensors is the same (the experimental uncertainty has been quantified by the bracket of the traces of the two sensors). For this reason, the representation of the target temperature without the initial offset has also been adopted, see figure 8 (c)-(d). Comparing the traces of the two leads, except for the initial stabilization before the current pulses, once the offset has been removed, the measurements are very similar (not shown), meaning that the two CLs are reacting in the same way to the driver.

The computed values on the CL1 and CL2, see figure 8, are in very well agreement with the experimental traces (the error bar on the computed results reflects the error bar on the computed R_C). This shows that, not only the heat capacities, but also the heat paths are correctly modelled, since both the amplitude as well as the peaks of temperature match with the experiments within the error bar.

7.2. Heat loads

The opportunity to compare also the data of the heat loads coming from the environment (warm end heat load) and the one exiting from the cold end (cold end heat load) is one of the advantages of having a more complete dataset, with respect to, for example, the one employed in [13].
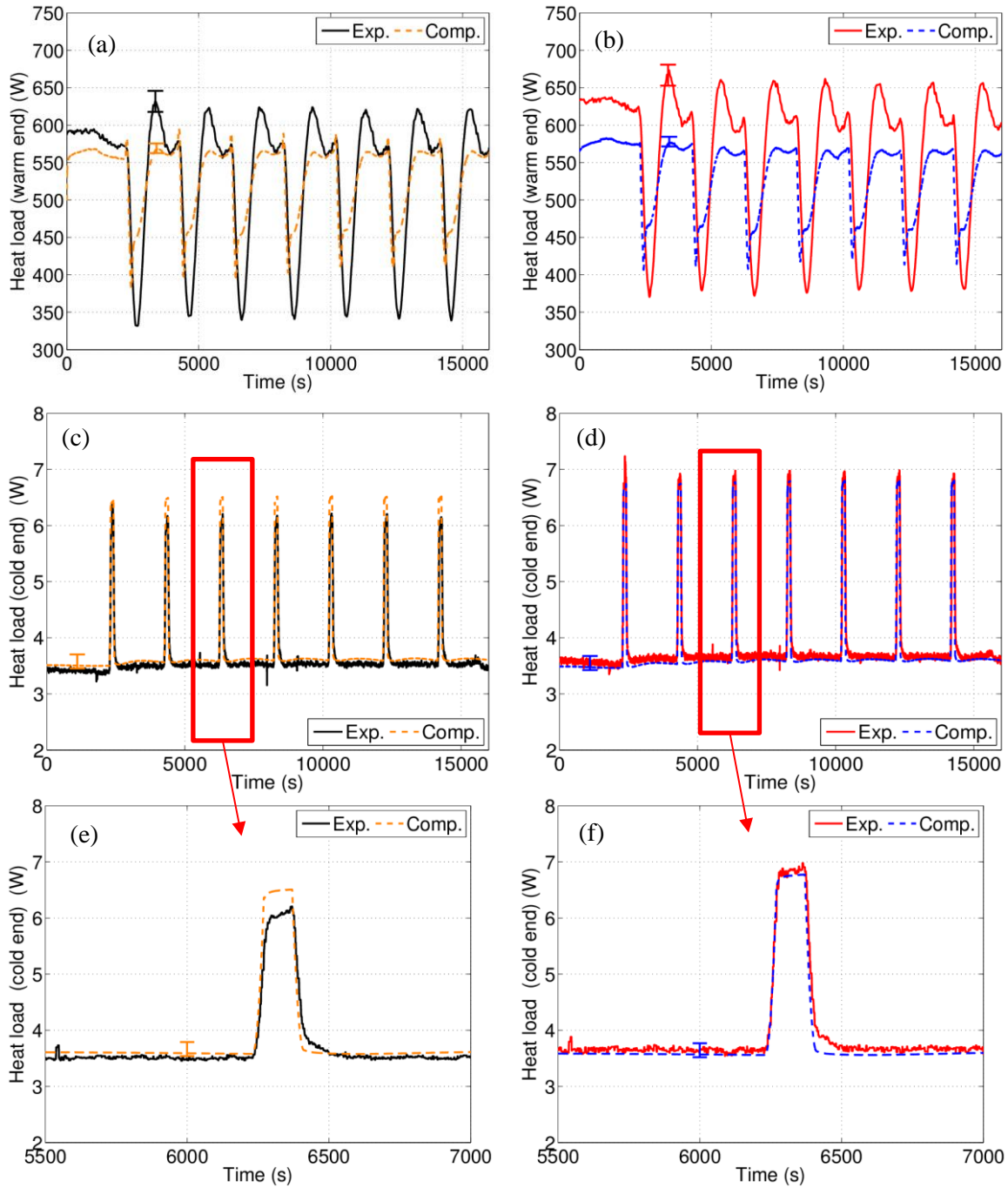
Figure 9. Simulation of the JT-60SA CLs pulsed test: measured (solid lines) and computed (dashed lines) heat load evolution at the warm and cold ends of the CL1 (a), (c) and CL2 (b), (d). The zoom on the first pulse in CL1 (e) and CL2 (f) are also shown.

In figure 9, we present the measured values of heat loads and their comparison with the computed values. The measured CL1 warm end heat load is constantly greater than the CL2 one by an almost constant value of 40 W, while the cold end ones are much closer, except during the current pulse, when the CL1 cold end heat load is ~ 1 W smaller with respect to the CL2 one, due to the smaller contact electrical resistance present in the CL1 cold endcap.

The measured warm end heat load is actually the power of the heaters placed at the RT, whose aim is to keep as flat as possible the temperature gradient in order to avoid considerable amount of heat leakage inside the lead from the external environment.

Since the computation starts at the temperature sensor location, which is located downstream with respect to the heater location, the spatial temperature profile of the copper includes a non-zero value of the gradient at the RT end, from which the heat leakage from environment to the lead can be computed. This can be seen as the heater power needed to have zero gradient, but of course only a qualitative agreement can then be achieved between measured and computed values of warm end heat load, simply because it is not ensured that the measured heater power is such that the gradient at RT is exactly zero and the contribution of the water cooling of the power cables connected to the RT end cannot be quantified, since no measurements were performed on that cooling circuit.

The comparison between the computed heat load at the warm end for both leads shows a smaller difference with respect to the experimental one. This is because the load in that location can be strongly affected by the water-cooled power cables, which are not present in the model.

The cold end heat load is measured calorimetrically, through the data provided on the enthalpy and mass flow rate of the He used to cool the cold end region, which is fed at cryogenic temperature (i.e., it is not the same He stream that cools the HX). The computed value is obtained summing two contributions: the one coming from the copper and a non-negligible additional portion coming through the vacuum shell, see figure 7. A very good agreement with the measured values is found; also the higher cold end heat load peak values of the CL2 are well reproduced, since the higher value of the electrical resistance at the cold endcap is properly taken into account.

7.3. Pressure drop

In figure 10, the pressure drop measured across the HX is compared to the computed one, showing that the latter underestimates as expected the measured valued by a ~ constant value. The offset is very similar to the one present in the steady state cases #2 of figure 6, since the mass flow rate during the entire transient is ~ constant and similar to the steady state one. Apart from the offset, the measured trend is well reproduced by the computed values: since the measured mass flow rate was used as input of the model, this qualitatively confirms the pressure drop model (friction factor correlations) used in CURLEAD.
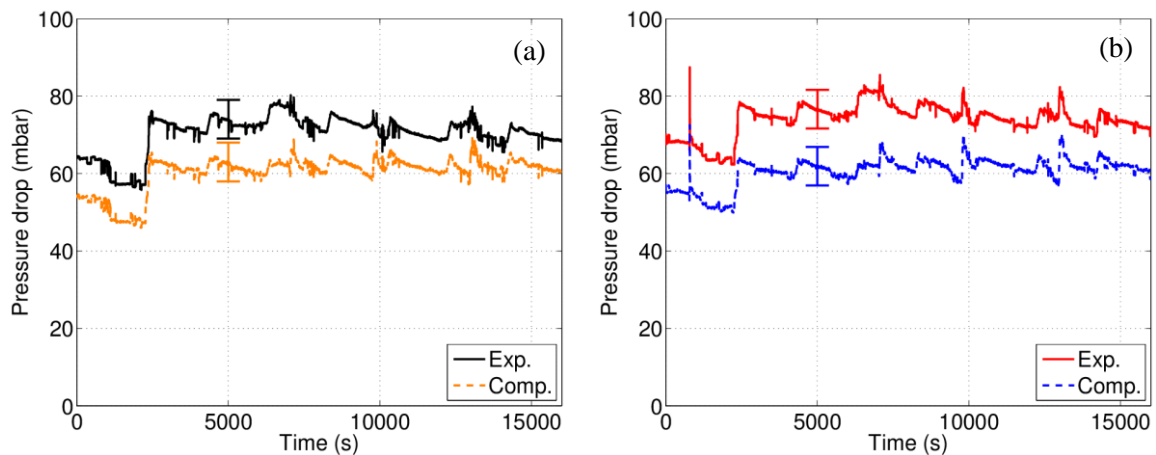

Figure 10. Simulation of the JT-60SA CLs pulsed test: comparison of the measured and the computed GHe pressure drop evolution for the CL1 (a) and CL2 (b).

7.4 Global energy balance

The energy conservation per unit time for the Cu bar reads:

$$\rho c(T) \cdot V \frac{dT}{dt} = q_{gen} + q_{Cu} + q_{top} - q_{bot} - q_{He} \qquad [W] \qquad (3)$$

where $\rho c(T) \cdot V \frac{dT}{dt}$ is the variation of the total internal energy of the conductor (ρ is the density, c the specific heat, V the volume, T the temperature and t the time), q_{gen} is the power generated through Joule effect when current flows through the resistive parts of the conductor, q_{Cu} is the conductive power transferred to the conductor by the shells through the region in which they are in contact, q_{top} is the power entering the CL from its warm end by conduction, q_{bot} is the power exiting the CL from the cold end by conduction, q_{He} is the power removed by the helium flow. All the quantities are time dependent. Similar energy balances can be written for the other region of the CL (HTS).

The major role in terms of stored energy is played by the conductor, mainly due to its large mass, especially in the HX region. The evolution of the experimental variation of the conductor internal energy (evaluated summing up the different contribution at the right-hand side of (3)) shows a trend to slightly decrease during the pulses - the time behavior of the leads looks slightly different which is due to the different initial conditions before the first current pulse.

Looking at the computed variation of internal energy in figure 11, a periodic behaviour in the variation of energy stored in the conductor is apparently reached, see figure 11(a). Although seven current pulses did not allow reaching a completely periodic behaviour of the vacuum shell, see figures 11(c) and 11(d), the internal energy stored therein is two order of magnitudes smaller than in the conductor and one order of magnitude smaller than in the HX shell, resulting in a negligible overall impact.
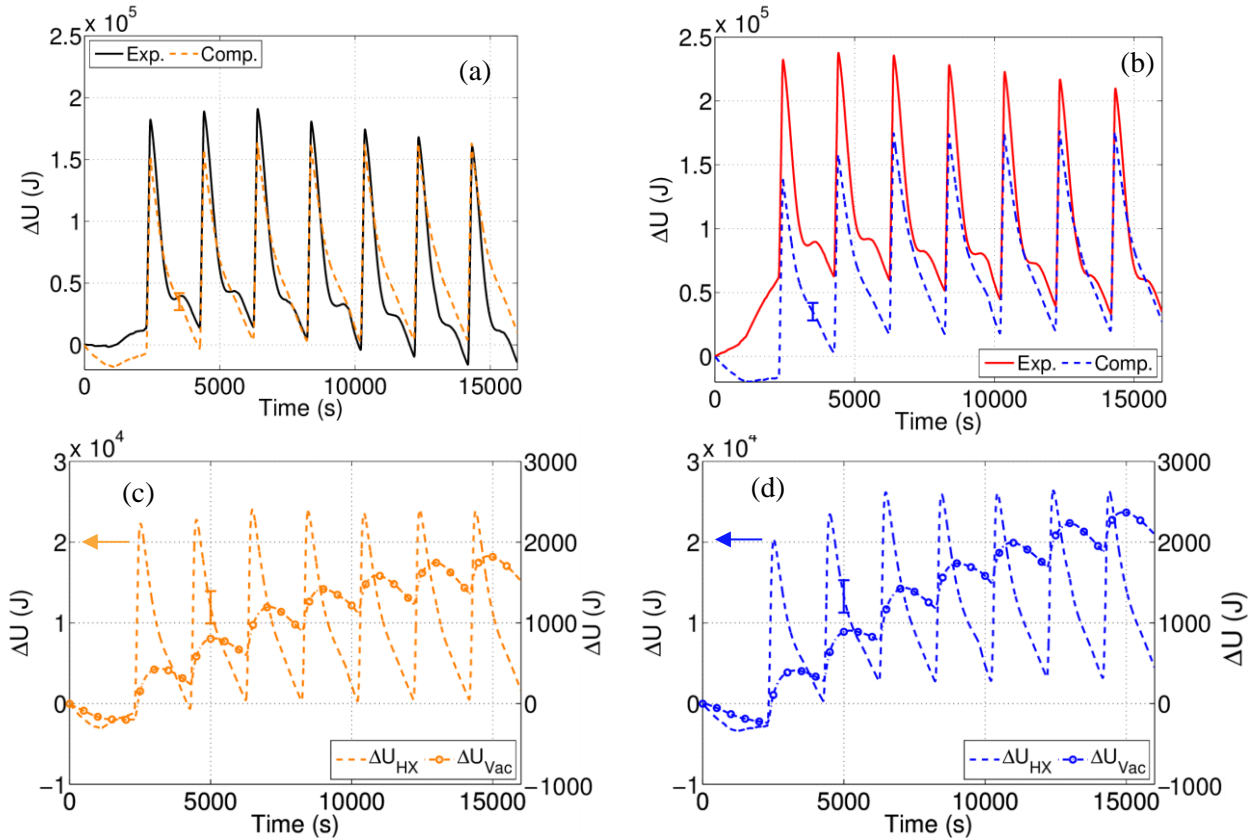
Figure 11. Simulation of the JT-60SA CLs pulsed test: evolution of the variation of the internal energy for the conductor of CL1 and CL2 (a), (b). Evolution of the variation of the internal energy for the CL1 and CL2 vacuum shell and HX shell in (c) and (d), respectively. In (a) and (b), also the experimental value is reported.

8. Conclusions and perspective

The thermal-hydraulic features of the steady-state and transient measurements of the JT-60SA HTS CL, tested at KIT prior to their shipping to Japan has been analysed using the CURLEAD code.

The fundamental new ingredients needed in the model to cope with the JT-60SA geometry were identified as the shells present in the CL structure and acting as thermal bridges between environment and cold end, which have been now implemented in an updated version of the CURLEAD code.

Both in steady-state and transient operation, the computed target temperature evolution matches with experimental values if all the thermal bridges present in the CL are considered. The main effect of the shells come from the heat transferred by conduction, rather than by their additional heat capacity: an insight into the computed solution allowed understanding the small role played by the heat capacity of the two shells, compared to that of the copper conductor.

In the future, we plan to use the new CURLEAD version to analyse the forthcoming test of the new KIT HTS CL design equipped with REBCO tapes.

Acknowledgments

References

[1] Heller R, Hull J R 1995 Conceptual design of a forced-flow cooled 20kA current lead using Ag-alloy sheathed Bi-2223 high temperature superconductors *IEEE Transactions on Magnetics* **5(2)** 797-800

[2] Heller R, Fietz W H, Kienzler A and Lietzow R 2011 High Temperature Superconductor Current Leads for Fusion Machines *Fusion Engineering and Design* **86** 1422–6

[3] Zhou T, Ding K, Liu C, Bi Y and Song Y 2015 R&D on 52-kA HTS Current Lead at ASIPP *IEEE Transactions on Applied Superconductivity* **25(2)** 1-4

[4] Ballarino A 2002 Current leads for the LHC magnet system *IEEE Transactions on Applied Superconductivity* **12(1)** 1275-80

[5] Wesche R and Fuchs A M 1994 Design of superconducting current leads *Cryogenics* **34(2)** 145-54

[6] Gavrilin A V et al. 2002 Comparative Analysis of Design Options for Current Leads for Wendelstein 7-X Magnet System *IEEE Transactions on Applied Superconductivity* **12(1)** 1301-04

[7] Wu S et al. 2007 An overview of the EAST project **82(15-24)** 463-71

[8] Marshall W S et al. 2014 Design of N2 Cooled Bi-2223 HTS Current leads for Use in 0.4T Field for the NHMFL Series-Connected Hybrid Magnet *Advances in Cryogenic Engineering* **1573(1)** 1018-1025

[9] Kamada Y, Barabaschi P, Ishida S and The JT-60SA Team and JT-60SA Research Plan Contributors 2013 Progress of the JT-60SA project *Nuclear Fusion* **53** 104010

[10] Isono T, Hamada K and Okuno K 2006 Design optimization of a HTS current lead with large current capacity for fusion application *Cryogenics* **49(9)** 683-7

[11] Ballarino A 2007 HTS Current Leads: Performance Overview in Different Operating Modes *IEEE Transactions on Applied Superconductivity* **17(3)** 2282-5

[12] Lewandowska M and Wesche R 2013 Parametric study for the cooling of high temperature (HTS) current leads *Cryogenics* **53** 31-6

[13] Heller R, Bauer P, Savoldi L, Zanino R and Zappatore A 2016 Predictive 1D thermal-hydraulic analysis of the prototype HTS current leads for the ITER correction coils *Cryogenics* **80(3)** 325-32

[14] Fietz W H, Heller R, Kienzler A and Lietzow R 2009 High temperature superconductor current leads for Wendelstein 7-X and JT-60SA *IEEE Transactions on Applied Superconductivity* **19(3)** 2202-5

[15] Heller R 1989, Numerical calculation of current leads for fusion magnets. KfK 4608 Karlsruhe

[16] Rizzo E, Heller R, Savoldi Richard L and Zanino R 2013 Computational thermal-Fluid Dynamics analysis of the laminar regime in the meander flow geometry characterizing the heat exchanger used in the High Temperature Superconducting current leads *Fusion Engineering and Design* **88(11)** 2749-56

[17] Rizzo E, Heller R, Savoldi Richard L and Zanino R 2013 CtFD-based correlations for the thermal–hydraulics of an HTS current lead meander-flow heat exchanger in turbulent flow *Cryogenics* **53** 51-60